Available online at www.sciencedirect.com
SCIENCE DIRECT®
Acta Materialia 53 (2005) 4795–4800
Acta MATERIALIA
www.actamat-journals.com

The difference of phase distributions in silicon after indentation with Berkovich and spherical indenters

I. Zarudi [a], L.C. Zhang [a,*], W.C.D. Cheong [a], T.X. Yu [b]

[a] School of Aerospace, Mechanical and Mechatronic Engineering, The University of Sydney, NSW 2006, Australia
[b] Department of Mechanical Engineering, Hong Kong, University of Science and Technology, Clear Water Bay, Kowloon, Hong Kong

Received 7 April 2005; received in revised form 27 June 2005; accepted 27 June 2005
Available online 24 August 2005

Abstract

This study analyses the microstructure of monocrystalline silicon after indentation with a Berkovich and spherical indenter. Transmission electron microscopy on cross section view samples was used to explore the detailed distributions of various phases in the subsurfaces of indented silicon. It was found that an increase of the P_{max} would promote the growth of the crystalline R8/BC8 phase at the bottom of the deformation zone. Microcracks were always generated in the range of the P_{max} studied. It was also found that the deformation zones formed by the Berkovich and spherical indenters have very different phase distribution characteristics. A molecular dynamics simulation and finite element analysis supported the experimental observations and suggested that the distribution of the crystalline phases in the transformation zone after indentation was highly stress-dependent.

Keywords: Nanoindentation; Silicon; Phase transformation; Stress

1. Introduction

Monocrystalline silicon as a principal material for semiconductor and photovoltaic technologies [1,2] has been a focus of an extensive research for more than a decade [3–20]. Various aspects of deformation characteristics induced by indentation have been analysed by different techniques such as in situ monitoring of electrical resistance [5,11,21] and acoustic emission [11], ex situ application of Raman spectroscopy [9,10,14,22] and transmission electron microscopy (TEM) on plan [3,11] and cross section view samples [6,7,10] and molecular dynamics simulations [23–26]. It has been demonstrated that the microstructure of silicon after indentation with a spherical indenter depends on the maximum indentation load (P_{max}) [7], loading/unloading speed [10] and number of applied stress cycles [13,14]. A larger P_{max} endorses crystalline phase transformation and crystal growth [19], while a high loading/unloading indentation speed promotes an amorphous phase [10,18]. A cyclic stress, on the other hand, leads to a gradual phase transformation [13,14]. The evolution of the crystalline phases have been found to be consistent with the distribution of the hydrostatic stress and commenced in the central part of the transformation zone [13,15,26,27]. Nevertheless, the point indenter induced microstructural changes has not received sufficient attention. For example, Mann et al. [8] concluded, with the aid of TEM on plan-view samples, that large contacts (larger P_{max}) endorse an amorphous phase [11]. However, both Raman spectroscopy and plan-view TEM cannot distinguish the phase changes inside the deformation zone along the vertical direction. As a result, location of the crystalline/amorphous phases and the details of their microstructure after an indentation with a Berkovich indentor have not been explored. The differences

* Corresponding author. Tel.: +612 9351 2835; fax: +612 9351 7060.
E-mail address: zhang@aeromech.usyd.edu.au (L.C. Zhang).

1359-6454/$30.00
doi:10.1016/j.actamat.2005.06.030

of the phase transformation zones caused by Berkovich and spherical indenters have not been understood sufficiently.

In the present study, we will use cross section view TEM to clarify the problem. In addition, a molecular dynamics simulation and finite element analysis will be used to assess the stress field generated in order to understand the difference in the final structures of the transformation zones observed in experiment.

2. Method

2.1. Experiment

The test material was a monocrystalline silicon (1 0 0) wafer. The Berkovich indenter used had a nominal radius of 250 nm. The indentations were conducted on a micro hardness tester (MHT Micro Photonics, USA). To capture the effect of the magnitude of indentation load, the study used three sets of maximum loads of $P_{max} = 20$, 50 and 90 mN. Fifty tests were performed for each P_{max}. In each cycle of an indentation the loading/unloading rate was 0.25 mN/s. A holding time of 30 s was used at 10% of the maximum load for thermal drift measurements followed by complete unloading.

Conventional TEM studies were carried out in a Philips CM12 transmission electron microscope, operating at 120 kV. The ⟨1 1 0⟩ cross section TEM specimens were prepared by a technique using a tripod [7]. In the preparation, the material removal was continuously monitored and the sample position with respect to the tripod was adjusted during the mechanical thinning. Finally, ion-beam thinning was carried out to provide a sufficiently thin area for the TEM investigations. At least three samples were prepared and at least seven to nine transformation zones were examined for every P_{max} studied.

2.2. Molecular dynamics and finite element analyses

The molecular dynamics method [26–29] enables one to understand the nano-mechanism affecting the nano-structural change in silicon and the finite element method can provide theoretical insight at a larger dimensional scale. Though molecular dynamics does not reproduce the real experiments due to differences in time and size scale, the simulation provides possible theoretical evidence of the phase transformation observed in the experiments and enables us to better understand the mechanisms involved in such a transformation process that transcend scale differences [23].

In this research, a molecular dynamics model composed of a silicon mono-crystal and a diamond indenter was created. A pyramidal indenter was used to simulate the Berkovich indenter. The dimension of the control volume of the silicon specimen was made sufficiently large (6.5 nm × 10.3 nm × 10.3 nm) to eliminate boundary effects. The maximum penetration depth of the indentation was 2 nm. To restrict the motion of the specimen, layers of boundary atoms that are fixed to space were used to contain the Newtonian atoms with the exception of the top (1 0 0) surface that is exposed to the indenter. Thermostat atoms were also used to ensure reasonable outward heat conduction away from the control volume. The silicon sample is made up of 148 280 atoms and the diamond indenter is made up of 1226 atoms. Previous research [25,26,28] has shown that the Tersoff potential [29] can be used to describe the interactions between the silicon atoms, and Morse potential [27,28] is suitable for interaction between the silicon and carbon atoms. In addition, it has also been shown that the Tersoff potential is applicable to the modelling of the different phases of silicon due to transformation. Detailed discussion of the molecular dynamics modelling can be found in Zhang and Tanaka [26,27].

The FEA simulations are performed with a Young's modulus of 80 GPa and a Poisson's ratio of 0.17 [30]. A 3D finite element model is created using ADINA 8.2 for the numerical solution of the nano-indentation on an elastic substrate with a spherical indenter and a Berkovich indenter of the same dimension as the experiment. The objective of the FEM simulation is not to obtain the exact stress distribution in silicon due to indentation but to obtain a qualitative figure of the general stress distribution in an elastic material to a Berkovich and spherical indenter. The mesh was designed so that the meshing is very fine near the indenter (in order to resolve the contact conditions and allow for accurate contact area determination). Accordingly, the mesh was chosen to be large enough for each calculation so that the results obtained were insensitive to the movement of the outer boundaries of the mesh. The size of the control volume is sufficient to eliminate any boundary effects. The penetration is simulated by gradually applying a downward displacement on the rigid indenter.

3. Results and discussion

3.1. Experimental findings

Fig. 1 shows the diffraction contrast images, demonstrating the morphology and microstructure of the transformation zones after the indentation tests with different P_{max}. The diffraction patterns were inserted to indicate the crystallinity inside the transformation zones. Fig. 1(a) presents the case with $P_{max} = 20$ mN. It shows that the transformation zone has a nearly triangular shape with a maximum depth of 340 nm.

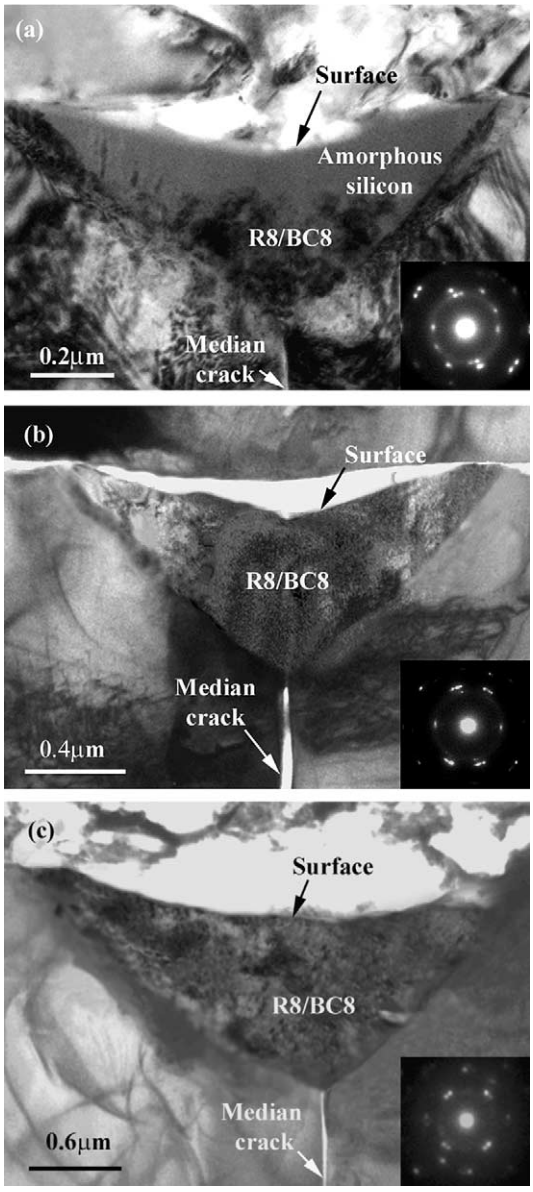

Fig. 1. Microstructure of the transformation zone after indentation with the Berkovich indenter (the diffraction patterns of the transformation zones are inserted): (a) $P_{max} = 20$ mN, (b) $P_{max} = 50$ mN, (c) $P_{max} = 90$ mN.

A residual indent of 130 nm deep is evident on the sample surface upon which the indenter impressed, indicating a significant plastic deformation. Also a median crack is emanating from the bottom of the transformation zone, while the presence of the crack at this low P_{max} was unexpected if the indenter was spherical [7,13,15,19]. An amorphous phase is obvious in the upper part of the zone. However, crystalline phases are located in the central part at the bottom of the transformation zone. The location of the crystalline phases is different from those formed in tests with a spherical indenter [7] and will be discussed later. These were identified as R8/BC8 phases (see inset in Fig. 1(a) and [19] for details).

In contrast, after indentation with $P_{max} = 50$ mN the whole transformation zone was occupied by R8/BC8 phases (see inset in Fig. 1(b)). The maximum depth of the zone grew to 600 nm and the residual impression depth became 360 nm. A median crack had clearly appeared.

The microstructure of the transformation zone $P_{max} = 90$ mN (Fig. 1(c)) was similar to the case of $P_{max} = 50$ mN. However, the size of R8/BC8 crystals grew from 120 to 300 nm (see Fig. 1(b) and (c)). Microcracks were noticeably developed. The maximum depth of the zone rose to 1100 nm and the residual surface impression went up to 850 nm.

Fig. 2 shows the load–displacement curves of the indentation tests described above. At $P_{max} = 20$ mN three types of load–indentation curves were detected from a total of 50 indentations, of which 10 are with

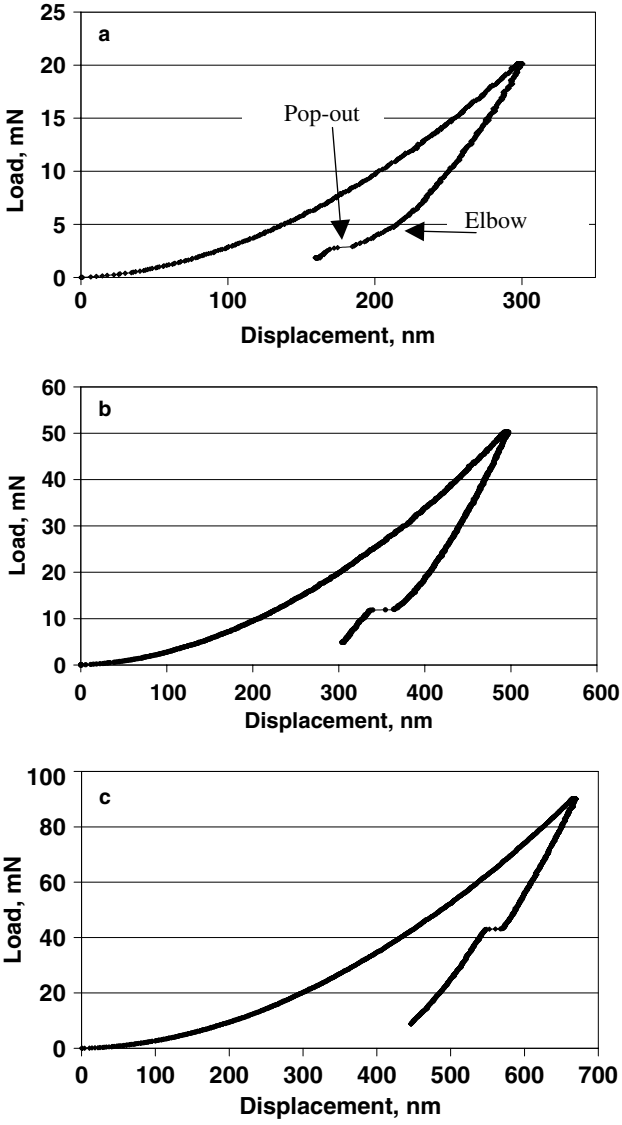

Fig. 2. Load–displacement curves with various maximum loads: (a) $P_{max} = 20$ mN, (b) $P_{max} = 50$ mN, (c) $P_{max} = 90$ mN.

elbows, 16 are with both pop-outs and elbows (see Fig. 2(a)) and the rest are with pop-outs only. Although the three types of load–displacement curves are different, the corresponding structures in all the transformation zones were very much similar to each other, i.e., they were composed of a mixture of amorphous and crystalline components; however, the quantity of the crystalline phase varied. The above observation indicates that the shape of the load–displacement curves (pop-out only, elbow only or a combination of them) does not reflect the distribution of the final phases in the transformation zone in position or volume percentage.

When indenting with $P_{max} = 50$ mN, two types of load–displacement curves were detected, of which 10 are with both pop-outs and elbows and 40 featured pop-outs only (Fig. 2(b)). No amorphous component was identified in the transformation zone, but the median crack was found to be longer and wider.

For the indentation with $P_{max} = 90$ mN, all the 50 load–displacement curves were with pop-outs only and the structure of all the transformation zones was completely crystalline.

3.2. Mechanism of the phase distribution variations

As mentioned in the previous section, the positions of the crystalline R8/BC8 phases found within the amorphous residual indentation zone are different in the case of indentation by a Berkovich or a spherical indenter. With a Berkovich indenter, the crystalline R8/BC8 phase is found at the bottom of the transformation zone. Whereas with a spherical indenter, the crystalline phases produced are found closer to the surface and appear in the middle of the transformation zone (Fig. 3) [13].

Since the formation of the R8/BC8 phases is strongly stress dependent, the different stress distributions due to the Berkovich and spherical indenters result in different R8/BC8 distributions within the transformation zone. The effects of various stresses that attribute to this difference are discussed in this section.

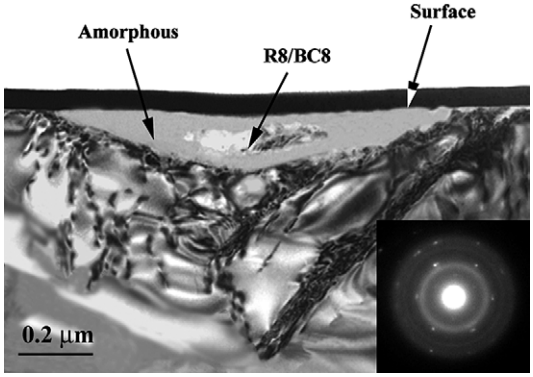

Fig. 3. Microstructure of the transformation zone after indentation with a spherical indenter ($P_{max} = 30$ mN, the radius of indenter = 5 μm) [13].

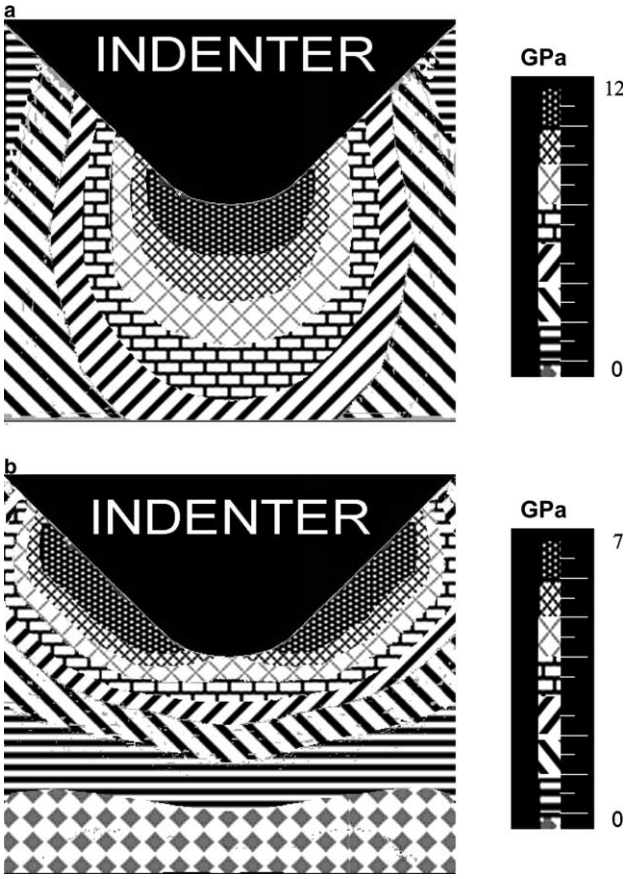

Fig. 4. Stress contours under Berkovich indenter obtained from finite element analysis: (a) hydrostatic, (b) octahedral. (The region of highest stress is represented by the darkest contour under the indenter.)

Fig. 4 shows the finite element stress contour plots of subsurface stresses under a Berkovich indenter at the maximum indentation load. The magnitudes of the stresses are not discussed as the focus here is the distribution of the highest stresses. A comparison between the hydrostatic stresses (see Fig. 4(a)), which are required to initiate the R8/BC8 phase, and the octahedral shear stress (see Fig. 4(b)), which necessitates the breaking of bonds leading to the formation of amorphous phase, reveals that in the case of indentation with a Berkovich indenter, the region with the highest hydrostatic stress is at the tip of the indenter, and is located below the high octahedral stress region, which is at the two sides of the indenter. This suggests that the R8/BC8 phase formed will be at the bottom of the transformation zone.

The molecular dynamics simulation gives the stress distributions with the amorphous zone formed due to indentation. Fig. 5 shows the residual amorphous indentation zone due to a pyramidal indenter. The shape of the residual amorphous zone is very close to that observed in experiment shown in Fig. 1(b).

Molecular dynamics simulation also reveals that in the case of the pyramidal indenter (similar to the Berkovich indenter), a high hydrostatic stress in the specimen

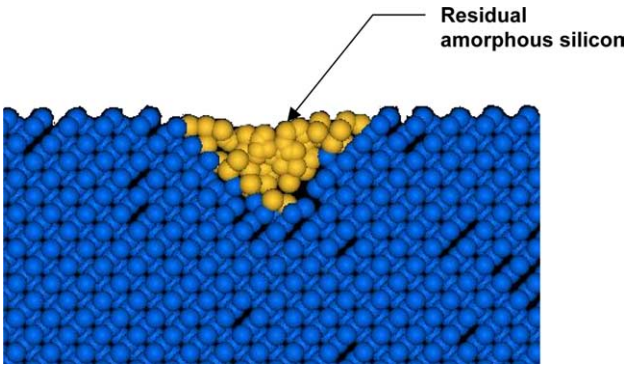

Fig. 5. Residual amorphous indentation zone obtained from molecular dynamics simulation.

at the maximum indentation (Fig. 6(a)) occurs beneath but close to the tip of the indenter. It is clear that the amorphous transformation zone (the shaded region) is mostly above the high hydrostatic stress area, defined by a critical value of the octahedral shear stress [26] as shown in Fig. 6(b). Hence, when the indenter unloads, the crystalline phase which forms in the region with high hydrostatic stresses will take place at the bottom of the amorphous zone.

Despite differences in scale, both the finite element and molecular dynamics simulations, show that in the case of a pyramidal indenter, the region of high hydrostatic stress occurs below the region of high octahedral stress. In addition, the molecular dynamics simulations also show that the region of high hydrostatic stress where R8/BC8 forms occurs at the bottom of the transformed amorphous zone. This seems to support well the experimental observation as shown in Fig. 1(a).

Fig. 7 shows the finite element stress contour plots of subsurface stresses under a spherical indenter at the maximum indentation load. In this case, the region of high hydrostatic stress (see Fig. 7(a)) is shallower than that of the high octahedral stress (see Fig. 7(b)). This suggests that the R8/BC8 phase should form in the location nearer to the surface and within the amorphous zone.

Fig. 8(a) presents the hydrostatic stress caused by a spherical indenter in a molecular dynamics model, which also shows that a spherical indenter produces higher hydrostatic stresses in the upper part of the amorphous transformation zone (defined by the shaded region of high octahedral stress), as show in Fig. 8(b).

Again, both the finite element and molecular dynamics analyses demonstrate that because of the difference in hydrostatic and octahedral stress distributions,

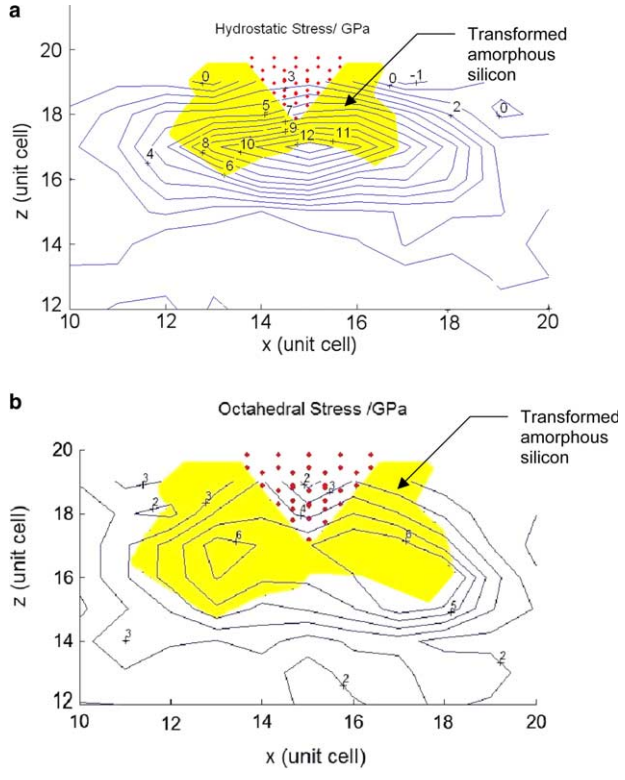

Fig. 6. Stress distribution at the P_{max} with a pyramidal diamond indenter from the molecular dynamics simulations (shaded region represents the transformation zone, dots represent diamond indenter): (a) hydrostatic, (b) octahedral.

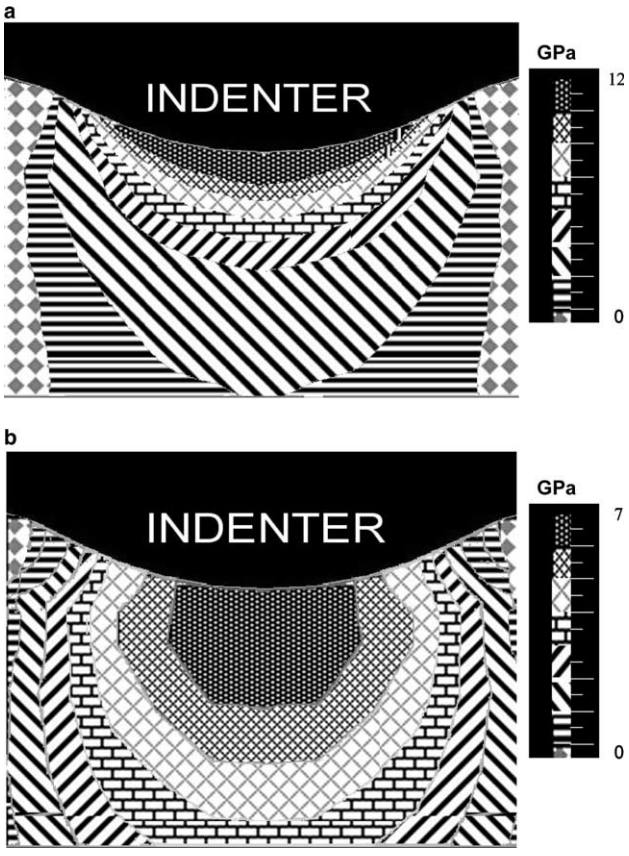

Fig. 7. Stress contours under a spherical indenter obtained from finite element analysis: (a) hydrostatic, (b) octahedral. (The region of highest stress is represented by the darkest contour under the indenter.)

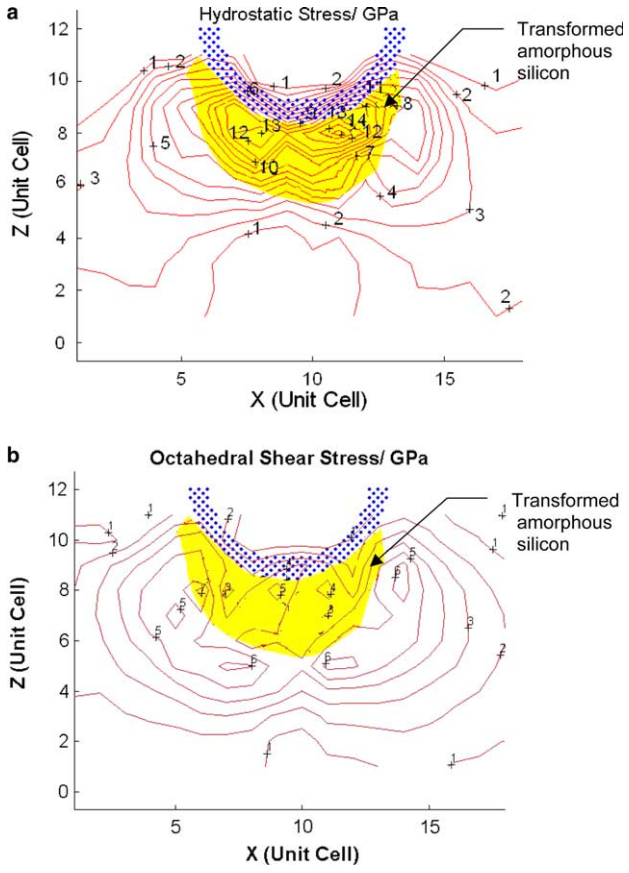

Fig. 8. Stress distribution at the P_{max} with a spherical diamond indenter from the molecular dynamics simulations (shaded region represents transformed amorphous zone, dots represent diamond indenter): (a) hydrostatic, (b) octahedral [25].

Berkovich and spherical indenters produce different distributions of R8/BC8 phases.

4. Conclusions

This study explores the distribution difference of various phases in silicon after indentation with a Berkovich and a spherical indenter. It can be concluded that:

1. an increase of P_{max} promotes more crystalline phases in the transformation zone;
2. the location of the crystalline phases is stress-dependent;
3. median cracks took place for all indentation tests conducted, which seems to play a role in altering the shapes of the load–displacement curves of the indentations;
4. elbows and pop-outs do not correspond accurately to the distribution of the final phases in the transformation zone, in position or in volume percentage.

References

[1] Deb SK, Wilding M, Somayazulu M, McMillan PF. Nature 2001;414:528.
[2] Blanco A, Chomski E, Grabtchak S, Ibisate M, John S, Leonard SW. Nature 2000;405:437.
[3] Clarke DR, Kroll MC, Kirchner PD, Cook RF. Phys Rev Lett 1988;60:2156.
[4] Pharr GM, Oliver WC, Clarke DR. Scripta Metall 1989;23:1949.
[5] Pharr GM, Oliver WC, Clarke DR. J Electr Mater 1990;19:881.
[6] Wu YQ, Yang XY, Xu YB. Acta Mater 1999;47:2431.
[7] Zarudi I, Zhang LC. Tribol Int 1999;32:701.
[8] Mann AB, Heerden Dv, Pethica JB, Weihs TP. J Mater Res 2000;15:1754.
[9] Domnich V, Gogotsi YG, Dub SN. Appl Phys Lett 2000;76:2214.
[10] Bradby JE, Williams JS, Wong-Leung MV, Swain MV, Munroe P. J Mater Res 2001;16:1500.
[11] Mann A, van Heerden D, Pethica J, Bowes P, Weihs T. Philos Mag A 2002;82:1921.
[12] Tachi M, Suprijadi S, Arai S, Saka H. Philos Mag 2002;82:133.
[13] Zarudi I, Zhang LC, Swain MV. J Mater Res 2003;18:758.
[14] Zarudi I, Zhang LC, Swain MV. Appl Phys Lett 2003;82:1027.
[15] Zarudi I, Zou J, Zhang LC. Appl Phys Lett 2003;82:1027.
[16] Grillo SE, Ducarroir M, Nadal M, Tournie E, Faurie JP. J Appl Phys D 2004;36:L5.
[17] Pajares A, Chumakov M, Lawn BR. J Mater Res 2004;19:657.
[18] Zarudi I, Zou J, McBride W, Zhang LC. Appl Phys Lett 2004;85:932.
[19] Zarudi I, Zhang LC, Zou J, Vodenitcharova T. J Mater Res 2004;19:332.
[20] Zarudi I, Cheong WCD, Zou J, Zhang LC. Nanotechnology 2004;15:104.
[21] Gridneva IV, Milman YV, Trefilov VI. Phys Status Solidi 1972;14:177.
[22] Jang JI, Lance MJ, Wen SQ, Tsui TY, Pharr GM. Acta Mater 2005;53:1759.
[23] Cheong WCD, Zhang LC. Nanotechnology 2000;11:173.
[24] Cheong WCD, Zhang LC. J Mater Sci Lett 2000;19:439.
[25] Zhang LC, Tanaka H. Tribol Int 1998;31:425.
[26] Zhang LC, Tanaka H. JSME Int J, Series A: Solid Mech Mater Eng 1999;14:546.
[27] Zhang LC, Tanaka H. Wear 1997;211:44.
[28] Cheong WCD, Zhang LC. Key Eng Mater 2003;233–236:603.
[29] Tersoff J. Phys Rev B 1989;39:5566.
[30] Vodenitcharova T, Zhang LC. Int J Solid Struct 2003;40:2989.